Hernández-Vega et al

Appendix Notes S1-S8

Appendix Figures and Legends S1-S9

Appendix References

Appendix Note S1. Theoretical kymograph

During epiboly, the speed along the animal to vegetal axis, quantified in terms of the angle φ with respect to the animal pole decreases exponentially from the EVL margin while the components of the speed along the other two spherical coordinates r, and θ are null (**Figure 1b**).

$$v_\varphi = v^* \cdot e^{-(\varphi-\varphi^*) / \delta\varphi} \quad (9)$$

for $\varphi > \varphi^*$

$v_r = 0$

$v_\theta = 0$

with v* being the velocity of the EVL margin.

Taking this into consideration, we defined a characteristic length R and δφ, the width of the E-YSL, and derived the strain rates in the longitudinal and latitudinal directions in spherical coordinates (r, φ, θ)

$$e_{\varphi\varphi} = 1 / R \cdot \partial v_\varphi / \partial\varphi + v_r / R = - v^* / R\, \delta\varphi \cdot e^{-(\varphi-\varphi^*) / \delta\varphi} \quad (10)$$

$$e_{\theta\theta} = 1 / R \sin\varphi \cdot \partial v_\theta / \partial\theta + v_r / R + v_\varphi \operatorname{cotan}\varphi / R = v^* / R \cdot \operatorname{cotan}\varphi \cdot e^{-(\varphi-\varphi^*) / \delta\varphi} \quad (11)$$

From the volume conservation in the fluid,

$$e_{rr} = - e_{\varphi\varphi} - e_{\theta\theta} = v^* / R \cdot (1/\delta\varphi - \operatorname{cotan}\varphi) \cdot e^{-(\varphi-\varphi^*) / \delta\varphi} \quad (12)$$

Then the stress tensors, for a Newtonian viscous fluid, in longitudinal and latitudinal directions are (Guyon, Hulin et al., 2001)

$$\sigma_{\varphi\varphi} = - p + 2\, e_{\varphi\varphi} \quad (13)$$

$$\sigma_{\theta\theta} = - p + 2\, e_{\theta\theta} \quad (14)$$

and their difference, in the case under study, is

$$\sigma_{\varphi\varphi} - \sigma_{\theta\theta} = 2\,(e_{\varphi\varphi} - e_{\theta\theta}) = - 2 \cdot v^* / R \cdot (1/\delta\varphi + \operatorname{cotan}\varphi) \cdot e^{-(\varphi-\varphi^*) / \delta\varphi} < 0 \quad (15)$$

Note that the sign of the term (1 / δφ + cotanφ) is opposite to the sign of the difference $\sigma_{\varphi\varphi} - \sigma_{\theta\theta}$. For a constricting area of a maximum width of 100 μm, as experimentally determined for the E-YSL, the latitudinal stress will always be larger than the longitudinal stress from the beginning of epiboly until closure (**Appendix Figure S8**).

To calculate the strain rates throughout the EVL cells, we consider them as an elastic spherical cap at equilibrium centered on the animal pole. Thus, the rate of deformation

of the surface is the same at each point of the EVL surface. The surface A_φ of this spherical cap extending up to the angle φ is

$$A_\varphi = 2\pi R^2 . (1 - \cos\varphi) \quad (16)$$

and its rate of change

$$dA_\varphi / A_\varphi = \sin\varphi / (1 - \cos\varphi) . d\varphi \quad (17)$$

To maintain the elastic equilibrium state, this quantity should be constant for all φ and, for φ*, equal to the angle of the margin of the EVL

$$dA_\varphi / A_\varphi = dA_{\varphi^*} / A_{\varphi^*} \quad (18)$$

$$\sin\varphi / (1 - \cos\varphi) . d\varphi / dt = \sin\varphi^* / (1 - \cos\varphi^*) . d\varphi^* / dt \quad (19)$$

thus, the speed at the different coordinates can be expressed as

$$v_\varphi (\varphi) = \sin\varphi^* / \sin\varphi . (1 - \cos\varphi) / (1 - \cos\varphi^*) . v^* \quad (20)$$

for $\varphi < \varphi^*$

$v_r = 0$

$v_\theta = 0$

The strain rate components along the longitudinal axis $e_{\varphi\varphi}$ and latitudinal axis $e_{\theta\theta}$ at the EVL surface is

$$e_{\varphi\varphi} = 1 / R . \partial v_\varphi / \partial\varphi + v_r / R = v^* / R . 1 / \sin^2\varphi . (1 - \cos\varphi) / (1 - \cos\varphi^*) \quad (21)$$

$$e_{\theta\theta} = 1 / R . \sin\varphi . \partial v_\theta / \partial\theta + v_r / R + v_\varphi . \cot\varphi / R = v^* / R . \cos\varphi / \sin^2\varphi . (1 - \cos\varphi) / (1 - \cos\varphi^*) \quad (22)$$

and from volume conservation,

$$e_{rr} = - e_{\varphi\varphi} - e_{\theta\theta} = - v^* / R . 1 / (1 - \cos\varphi^*) < 0 \quad (23)$$

The rate of deformation in the radial direction, e_{rr}, should be equal for all the EVL cells. Indeed, at any stage the width of the EVL is uniform as observed by 2-photon microscopy.

We then calculated the difference between the stress tensor components in longitudinal and latitudinal directions in the EVL, that is

$$\sigma_{\varphi\varphi} - \sigma_{\theta\theta} = 2 (e_{\varphi\varphi} - e_{\theta\theta}) = 2 . v^* / R . 1 / \sin^2\varphi . (1 - \cos\varphi)^2 / (1 - \cos\varphi^*) > 0 \quad (24)$$

with the longitudinal stress always larger than the latitudinal stress in the EVL.

As the EVL margin progresses after 50% epiboly at a constant speed along the z-axis

$$v^* = v_0 / \sin\varphi^* \quad (25)$$

with v_0 being the speed at 50%. Then considering the velocity distributions in the EVL

$$v_\varphi(\varphi) = \sin\varphi^* / \sin\varphi \,.\, (1 - \cos\varphi) / (1 - \cos\varphi^*) \,.\, v^* \quad (26)$$

for $\varphi < \varphi^*$

and at the surface of the yolk

$$v_\varphi = v^* \,.\, e^{-(\varphi-\varphi^*) / \delta\varphi} \quad (27)$$

for $\varphi > \varphi^*$

we drew a theoretical kymograph along the surface, from animal to vegetal that was over-imposed to experimental kymographs obtained by two-photon microscopy (**Figure 1c**).

Appendix Note S2. Hydrodynamic Regression

Theoretical Considerations

A quasi-2D and purely elastic material of finite size immersed in a highly viscous fluid will progressively reach its elastic equilibrium and dissipate the elastic energy it could store by producing flows in the surrounding viscous fluids. The dynamics of the system is governed by hydrodynamics at low Reynolds numbers. The observed flows in the fluid mirror the out-of-equilibrium stresses at the interface with the elastic material.

Following these considerations, HR assumes that any cortical surface of living organisms can be described as a mesoscopic continuous quasi-2D elastic structure embedded in a viscous liquid. The stress and velocity continuity at the cortical-liquid interface allows to infer cortical elastic stresses from the stresses estimated within the surrounding fluids.

At equilibrium the cortical elastic stresses satisfy a local force balance

$$\square\square_{ij} / \square x_j = 0 \quad (28)$$

where $\square_{ij}$ are the components of the Cauchy stress tensor and x_j the j component of the position vector. Repeated indices follow the Einstein convention. Further, as the cortex is narrow, of width δh (with $\delta h << R$, the radius of a spherical embryo), we can

integrate the local force balance (Equation 28) perpendicular to the cortex δx_n, leading to

$$\partial \sigma_{tt} / \partial x_t = - \delta \sigma_{tn} / \delta h \qquad (29)$$

expressing the change in the stress along δx_t parallel to the cortex. Equation 29 relates the change of the longitudinal stress along the cortex σ_{tt} to the difference in tangential stress $\delta \sigma_{tn}$ at the two sides of the cortical membrane. The effective local surface tension in the cortex τ can then be calculated from Equation 29

$$\partial / \partial x_t (\delta h \, . \, \sigma_{tt}) = - \delta \sigma_{tn} \qquad (30)$$

$$\tau = \delta h \, . \, \sigma_{tt} \qquad (31)$$

Thanks to the continuity of the tangential stresses at the cortex / fluid interface and considering that there is no normal displacement of the cortex surface, σ_{tn} is equal to the shear stress due to the shear viscosity ν

$$\sigma_{tn} = \nu \, . \, \partial v_t / \partial x_n \qquad (32)$$

where v_t is the tangential velocity.

Since tissues are surrounded by a liquid medium, any imbalance ($\partial / \partial x_t \, \tau \neq 0$) in the cortex tension τ, e.g. due to the contraction or stretching on the cortex surface associated to a morphogenetic process, will induce a variation of the fluid stresses at the two sides of the membrane and create a discontinuity of the shear flow in the surrounding viscous fluids. It is then possible to trace back the relative surface cortical tension τ, up to an additive constant by analyzing the fluid velocity field. This involves determining the fluid stress at the cortex using Equations 29 and 31. In other words, the measurement of the shear flow of the viscous fluid on both sides of any cortical surface let us inferring the quantitative profile of the surface tension along the cortex.

Hydrodynamic Regression

Fluid stresses can be indirectly estimated by fitting simulated velocity fields to experimentally measured velocity fields. From the fluid stresses we can retrieve the complete stress tensor at the cortical interface.

This procedure is implemented through regression analysis and by using analytical solutions of the dynamics of an incompressible viscous Newtonian fluid with negligible

inertia. This dynamics is governed by the volume continuity Equation 1, ensuring volume conservation, and the linear Stokes Equation 2:

$$\mathrm{div}\ \mathbf{V} = 0 \qquad (1)$$

$$\nu\ \mathbf{\Delta V} = \mathbf{grad}\ P \qquad (2)$$

with ν the dynamic viscosity, **V** the velocity field, **Δ** the Laplace operator, **grad** the gradient and P the dynamic pressure.

Equation 2 can be formally re-expressed as Equation 28, describing a force balance in terms of the local fluid stress. For a Newtonian fluid it reads

$$\boldsymbol{\sigma_{ij}} = -P\ \boldsymbol{\delta_{ij}} + 2\ \nu\ e_{ij} \qquad (33)$$

where $\boldsymbol{\delta_{ij}}$ stands for the Kronecker delta and $e_{ij} = (\partial v_i / \partial x_j + \partial v_j / \partial x_i) / 2$ (in Cartesian coordinates) is the strain rate tensor.

This Newtonian description of dynamics at low Reynolds number can be generalized to non-Newtonian fluids or to viscoelastic materials, which exhibit an initial linear response of their strain rate to stress when these are small enough. The overdamped dynamics allows us to derive forces responsible for the kinematics once we specify the constitutive relation that characterizes the mechanical response of the embedding liquids. Further, the Stokes equation is independent of time, so the flow depends on the instantaneous forces acting at the same instant. The Stokes equation provides a unique solution for the dynamic pressure field for a given velocity field. For a non-Newtonian liquid, for which memory effects become dominant, a generalized treatment of Equation 2 would be required. Otherwise, we can exploit the linearity and locality of Stokes equation to express the fluid velocity as a sum of elementary known solutions. This approach simplifies considerably the regression to obtain a theoretical approximation to the measured velocity field.

Fitting an analytical solution of the 3D velocity field increases significantly the precision in the spatial derivations and enables to compute the analytical dynamic pressure distribution. From the fluid velocity one can determine the corresponding fluid stress from Equation 33. Assuming that the fluid viscosity is constant or only slowly spatially varying (sharp variations are allowed at boundaries), we determined the variation of the local value of the tension at the embryonic cortex, τ using Equation 31, in both principal directions.

Finally, we defined and mapped a mechanical surface power density Π, the cortical elastic energy produced per unit of time and surface, responsible for the viscous flows observed. At any given moment, the surface power density Π supplied by the cortex at each point of its surface is opposite to the rate of change in internal cortical elastic energy density (**Figure 3c**) and can be derived from the measured stresses and strains in the fluid in contact with the cortex,

$$\Pi = - (\tau_{xx}\, e_{xx} + \tau_{yy}\, e_{yy} + 2\, \tau_{xy}\, e_{xy}) \qquad (34)$$

in local Cartesian coordinates in the plane tangent to the cortex surface. Π quantifies the cortical elastic energy released per unit of time and surface. From the analytic expression for the fluid flow one can also obtain the mechanical power density dissipated in the surrounding liquid.

Regression Analysis implementation

To perform the regression analysis and the modeling of the continuous elastic surface we first defined N_ε elementary solutions of Equations 1 and 2. Each elementary solution consists in a dipole to account for cortical stresses.

These dipoles are built as two Stokeslets pointing in opposite directions a distance δ away from each other (see **Figure 3b**) and distributed on a geometrical surface modeling the cortex. The separation distance, δ, is chosen of the order of the distance between neighbor dipoles, for simplicity. A Stokeslet provides the 3D velocity field, and corresponding pressure, created by a point force in a viscous fluid at low Reynolds numbers. Due to the linearity of the Stokes equation, the fluid velocity and pressure fields around the cortex can be expressed as a linear combination of the N_ε elementary solutions, $\mathbf{V_e}$ and p_e. Each solution e ($1 \leq e \leq N_\varepsilon$) is centered at a given position on a grid at the cortex and oriented perpendicularly to it. A multiplicative coefficient β_e was applied to each elementary solution. The independent variables of the regression are the coordinates of the grid points, X_e, Y_e and Z_e, and the dependent variables the coordinates of the grid velocity vectors $\mathbf{V^m_e}$.

For the regression, the fitting parameters are the coefficients β_e and the theoretical velocity field is written

$$\mathbf{V^f}(x, y, z) = \mathbf{V_0} + \sum_{1 \leq e \leq N\varepsilon} \beta_e \,.\, \mathbf{V_e}(x, y, z) \qquad (35)$$

with $\mathbf{V_0}$ a uniform velocity field.

As the solutions are analytical, each velocity field has a known associated analytical pressure field:

$$p^f(x, y, z) = \Sigma_{1 \le e \le N\varepsilon} \beta_e \, . \, p_e(x, y, z) \quad (36)$$

If the magnitude of the fluid viscosity is not known, the relative stress and dynamic pressure fields can still be derived absorbing the viscosity as a multiplicative factor.

The mean square error of the regression (Fisher, 1922) is then:

$$MSE = \sum_{1 \le e \le N\varepsilon} (\mathbf{V}^{\mathbf{f}}_{\mathbf{e}} - \mathbf{V}^{\mathbf{m}}_{\mathbf{e}})^2 / (N_{var} - N_{param}) \quad (37)$$

with N_{var} the number of independent variables $\{X_e\}$ and $\{Y_e\}$ and N_{param} the number of parameters $\{\beta_e\}$.

We randomly sampled the parameters $\{\beta_e\}$ and kept at each step the new value when it led to a decrease of the MSE. The sampling is repeated until MSE is smaller than a prescribed threshold or when a predefined number of iterations is reached.

The mean square error of the linear parameters estimate can then be written:

$$MSEP = MSE / \sum_{1 \le e \le N\varepsilon} [(X_e - X_m)^2 + (Y_e - Y_m)^2] \quad (38)$$

with X_m and Y_m the averages of the $\{X_e\}$ and $\{Y_e\}$ respectively.

To evaluate the quality of the simulation we calculated the

- relative mean square error of the velocity

$$RMSE = MSE / \sum_{1 \le e \le N\varepsilon} \mathbf{V}^{\mathbf{m}}_{\mathbf{e}}{}^2 \quad (39)$$

- relative mean square error of the pressure

$$RMSEP = MSEP / \sum_{1 \le e \le N\varepsilon} p_e^2 \quad (40)$$

- relative mean square error of the power, Π

$$RMSE\Pi = [MSE \, . \, MSEP]^{1/2} \quad (41)$$

The regression was performed iteratively by a Monte-Carlo simulation between measured and simulated velocity fields, guided by the mean square error (MSE). We applied this regression analysis to model a planar or a spherical active hydrodynamic cortex.

In the analysis, the PIV window sets a limit on the resolution of the estimated velocity field. Since the error in the velocity gradients estimate is proportional to the window size, because at low Reynolds numbers flows the stress is distributed over all the fluid domain, the inferred shear stress at the boundary will be reliable, provided that the ratio

of the PIV window size to the field size is equivalent or smaller than the relative fitting error. In fact, we found that for all our analyses this was always the case.

Planar modeling

To model a planar hydrodynamic cortex, we distributed multiple elementary solutions of the linear Stokes equation at different points of a planar 2D grid.

For the elementary solution e at coordinates x_e and y_e, the analytical velocity field at each point of coordinates x, y, z can be written as:

$$V^x_e(x, y, z) = \beta_e \, . \, [(x - x_e) \, . \, (z - z_0) / {R^+_e}^3 - (x - x_e) \, . \, (z + z_0) / {R^-_e}^3] \quad (42)$$

$$V^y_e(x, y, z) = \beta_e \, . \, [(y - y_e) \, . \, (z - z_0) / {R^+_e}^3 - (y - y_e) \, . \, (z + z_0) / {R^-_e}^3] \quad (43)$$

$$V^z_e(x, y, z) = \beta_e . \, [1/ R^+_e - 1/ R^-_e + (z - z_0)^2 / {R^+_e}^3 - (z + z_0)^2 / {R^-_e}^3] \quad (44)$$

with β_e being the fitting parameter and

$$R^+_e = [(x - x_e)^2 + (y - y_e)^2 + (z - z_0)^2]^{1/2} \quad (45)$$

$$R^-_e = [(x - x_e)^2 + (y - y_e)^2 + (z + z_0)^2]^{1/2} \quad (46)$$

The dynamic pressure would then be

$$p_e(x, y, z) = 2 \, . \, \nu \, \beta_e \, . \, [(z - z_0) / {R^+_e}^3 - (z + z_0) / {R^-_e}^3] \quad (47)$$

Employing Equation 33, from the dynamic pressure p and the strain rate tensors **e**, we can derive the liquid stress. Continuity of stresses at the tissue allows us to derive the cortical stress. From **σ** and **e**, we can also determine the surface power density, Π, a non-linear function of the power associated to each elementary velocity field. For an isolated elementary solution, regardless it models an active contraction or an active expansion, this power density is positive at the center and negative around it.

The elementary solutions of the PC model could be fitted directly to measured velocity fields (as described for the SC model), but also to measured 2D divergence fields (the 3D divergence of the velocity field vanishes due to the incompressibility of the fluid), which will precisely reflect contractions and expansions.

This approach was tested in the experimental analysis of the response to damage of the zebrafish yolk cortex. Here, actin and myosin are adjacent to the to the cortex and we assume they constitute the main motors of tissue deformations. The elementary solutions of the Stokes equation were positioned at each point of the measurements' PIV grid. This analysis leads to very small dissimilarities between measured and fitted

divergence fields. These minor differences could be due to intrinsic errors in the PIV measurements and the regression scheme. Thus, with high confidence, the fitted velocity field is the result of the active contractions taking place in the field of view.

Spherical modeling

To fit a 3D analytical field with cylindrical symmetry to measured 2D velocity fields, we designed circular solutions of the linear Stokes equation. They are the sum of elementary solutions for contraction and expansion regularly regularly positioned on a circumference. Each one of these solutions was oriented with the same relative angle to the axis of symmetry of the circle. To reconstruct the spherical shape, we distributed these circular solutions along one main axis, so that they draw one sphere with all elementary solutions pointing towards the center.

If R^s is the radius of the sphere s, z the coordinate along the main axis and φ the angle between the z-axis and the circle C^s_z, the radius of a circle C^s_z at z is $R^s . \sin\varphi$, and its circumference $2\pi . R^s . \sin\varphi$. For N_c circles, we set the number of elementary solutions on each to the closest integer to $(2 . N_c . \sin\varphi)$. At each of the poles ($\sin\varphi = 0$) we placed a single solution. Following this rule, we reached an approximately homogenous distribution of elementary solutions at the surface of the sphere. The convergence of the simulated velocity and pressure fields can be improved increasing the density of Stokeslets pairs distributed along the cortex.

The magnitude of each circular solution was controlled by a single parameter β^s_z. Moreover, a zero-order parameter β_0 was applied to a uniform flow in the direction of the symmetry axis. The parameters were randomly sampled. At each step of the fitting algorithm, the stochastic change of the parameters is rejected if the mean square difference between fitted and measured velocity fields increased. The algorithm reproducibly converged to an identical best fitting velocity field in the mean square sense. The dynamic pressure and the mechanical dynamic power were obtained following the same procedure applied to the planar analysis, although in spherical coordinates.

To test the predicted stress at the surface, we calculated the surface tension from the force balance that must be fulfilled at the boundary between the elastic cortex and the viscous fluid. We used Equation 29 of elastic equilibrium where $\delta\square_{tn}$, because of the

continuity of the tangential stresses, was calculated as the difference between the shear stresses in the fluid at the external and internal limits of the cortex. In addition, the continuity of the normal stresses was expressed by the Young-Laplace equation where surface tension due to membrane curvature relates to the difference between the external and the internal pressure δp. We could use directly the expression of the elastic equilibrium equation in spherical coordinates taking into account the curvature.

We can then plot the averaged surface tension τ along with the model prediction

$$\tau = - R \, . \, (\boldsymbol{\delta}p / 2 + \int d\varphi \, . \, \boldsymbol{\delta}\square_{tn}) \quad (48)$$

For the application of HR to the fluid droplet, one sphere of elementary solutions, distributed over $N_c = 16$ or $N_c = 31$ circles was positioned at the surface of the spherical droplet. It is important to note that the fluid droplet surface approaches zero dimensionality. HR provided a quasi-perfect fit of the internal velocity field of the fluid droplet to its analytical expression. Internal flows, pressure field and the two perpendicular main components of the elastic surface tension were readily estimated (see **Appendix Figure S4**). However, significant differences in the pressure map with the analytical solution were found at the surface (**Appendix Figure S4c**). We found that this discrepancy could be partially overcome by increasing the number (density) of elementary solutions in the model as described above.

For epiboly, the elementary solutions were distributed over $N_c = 16$ circles adjusted to the cortex sphere in parallel to the animal to vegetal pole axis. Upon fitting a refinement step was performed. This refinement consisted in doubling the number of circles located on the sphere (from 16 to 31).

Appendix Note S3. Flow Simulation Suite (SC flow fitting)

The HR code is provided in the two following links:

ftp://eservices.irbbarcelona.org/outgoing/adm/SCFlowSimulation_only_raw_data.zip

ftp://eservices.irbbarcelona.org/outgoing/adm/SCFlowSimulation.zip

The first file only includes the code, the raw data and the documentation. The second file also includes all intermediate and final results of the analysis with a representative

movie. From applying the second file retrieve the movies provided in ***Data/Results***.

Overview

The workflow is divided in three parts (Matlab scripts) that should be run sequentially:

1. PIV analysis: ***ZebrafishPIV.m*** located in the folder ***PIVAnalysis***
2. SC flow simulation and fitting: ***SimulationMain.m*** located in the folder ***FlowSimulation***
3. SC flow refinement: ***SimulationRefinement.m*** located in the folder ***FlowSimulation***

Please note that the code is only based on Matlab native functions so that no commercial toolbox is necessary. Still the workflow involves MAT PIV toolbox for the PIV analysis and the function Quiverc to plot color-coded vector fields. The necessary files are all included in the code release so that the code is self-contained. So far the code has only been tested under Matlab 2010b and Matlab 2012a.

MAT PIV toolbox: http://folk.uio.no/jks/matpiv/index2.html

Quiverc function: http://www.mathworks.com/matlabcentral/fileexchange/3225-quiverc

Datasets

A raw dataset and all associated intermediary and final results are provided in the folder ***Data***. This dataset consists in a single field of view two-photon microscopy time-lapse of the yolk granules taken with the settings described in the section “Live Imaging” of the Methods. In this dataset only the apparently best z slice has been kept (out of the three z slices that were acquired).

The raw images indexed by time frame can be found in the folder ***Data/Raw***.

Workflow

1. ImageJ pre-processing

For best results it is advised to pre-process the raw images with a detail-enhancing filter. We elected ImageJ FFT based bandpass filter and used the following settings: “Filter large structures down to 8 pixels”, “Filter small structures up to 5 pixels”, “Suppress stripes: None”, “Autoscale after filtering” and “Saturate image when autoscaling”.

To perform the filtering in ImageJ the easiest way is to import the raw images as an image stack from File > Import > Image Sequence…, then, apply the filter, and finally export the filtered images as a series of single tif images from File > Save as > Image Sequence…

Importantly the starting time frame index is 1 and 4 digits should be used for file naming. These frame indices are appended to the common root file name automatically by ImageJ on stack exportation.

The filtered images are provided in the folder ***Data/Filtered*** as reference.

2. Matlab PIV analysis (SimulationMain.m)

The user should first manually define three file paths (and root file names) before launching the script. This is performed by changing the value of some specific variables (all defined in the preamble of the .m file). These variables are:

1. *path* / *name2base*: The path to the filtered images folder / the root name of the filtered images (input, single Tiff .tif file)

2. *pathVisu* / *name2baseVisu*: The path to the raw images folder / the root name of the raw images (input, single Tiff .tif file)

3. *pathSave* / *name2baseSave*: The path to the folder used to save the flow simulation results / the root name of the main result file (output, Matlab .mat file).

The first and last time frames to be processed can be adjusted from the variables *FirstFrame*, and *LastFrame* before launching the script.

Note: Beside the .mat result file the script also generates two movies showing the original images with the PIV velocity field overlaid. The movie *PIV-…avi* displays the raw velocity field while the temporal filtered field is recorded in *moyTemps-…avi*. Both movies are stored in the results folder *pathSave*. These movies and the .mat results file can be found in the folder ***Data/PIV***.

3. Main flow simulation

Again the user should first configure several file paths + file names relative to the input/output of the scripts, these are defined in the variables:

1. PIVfile: The file generated from the previous step (input, .mat file, PIV results)

2. Resultsfile: The path and root name of the .mat files generated (one for each time frame) and holding the flow simulation results (output, .mat files, fitting results).

The user should also provide an estimate of the centre location and radius of the embryo (variables *xCentre*, *yCentre*, *rayonw*); defined in pixel units.

An estimate of the pole-to-pole tilting angle of the embryo (α) with respect to the horizontal should also be provided. This angle is expressed in radians and stored in the variable *angle*. A null angle corresponds to a situation where the animal pole is perfectly horizontally orientated and pointing to the left. As a convention we write these angles in the range [-2Pi ; 0] (see **Appendix Figure S9**).

Again the first and last time frames to be processed, as well as the frame step, can be adjusted from *FirstFrame*, *FrameStep*, and *LastFrame* before launching the script. *FrameStep* should be set to 1 unless you do not want to process all time frames.

While the fitting is iteratively improved, the simulation will display the simulated and measured (PIV) velocity fields, the Relative Mean Square Error between both fields and the pressure map. The refresh rate of these graphs can be configured from the variable *ShowGraph* (the default behavior is to plot the graphs only each 25 iterations). The fit is iteratively performed (up to 1800 iterations) for each time frame. On completion all the physical measurements estimated from the simulation are plotted to several graphs.

All the resulting .mat files (one per time frame) can be found in the folder ***Data/Fit***.

Simulation Refinement and Results

This script is used to improve the spatial accuracy of the flow simulation and generate the final results. The accuracy is improved by increasing the number of rings holding elementary solutions from 16 to 31. The script generates a movie of the power map overlaid to the original images as well as an animated graph summarizing the important physical measurements commented in the article.

First, some paths and file names have to be set from these variables:

FitFilePath: Folder+root name of the .mat files generated at step 2 (input, .mat files, fitting results)

RawFilesPath: Folder+root name of the raw images (input, single Tiff .tif files, raw images)

OutputPower: Path+filename of the mechanical power density map movie (output, uncompressed .avi)

OutputFig: Path+filename of the animated summary figure (output, uncompressed .avi).

The first and last time frames to be processed, as well as the frame step, can be adjusted from *FirstFrame*, *FrameStep*, and *LastFrame*.

Finally the minimum, maximum and isocontour step values used for the representation of the mechanical power density map as well as the minimum and maximum value for the velocity + stress summary figure can be adjusted. The resulting movies are found in the folder ***Data/Results***. A blue segment is overlaid on the mechanical power density maps. This segment is orientated towards the cortex point with highest tangential velocity (as estimated from the fitted analytical velocity field). The length of the segment indicates the pre-eminence of the maximum and is computed as the ratio of the maximum tangential velocity to the mean tangential velocity (scaled to a fourth of the radius).

Appendix Note S4. Mechanical power density and stress retrieval from Planar and Spherical Cortex Models

We applied HR to study the reaction of the external yolk membrane of the zebrafish embryo to the injury of its actomyosin cortex (a system for which the distribution of dynamic stresses and power density maps can be easily predicted) (**Appendix Figure S3**). We found that laser cuts of the yolk membrane underwent an initial transient relaxation followed by an extremely fast contraction that results in the immediate segregation of a shrinking central area and in the radial stretching of the surrounding external membranes (**Appendix Figure S3a** and **Video EV3**). The central area displayed a prominent accumulation of myosin (**Appendix Figure S3b**) indicating that its contraction constitutes an active process. Velocity fields were obtained by PIV from bright field transmission time-lapse videos of the yolk membrane and HR was performed by fitting 2D velocity divergence fields that provide a direct readout of the local contractions and expansions. Remarkably, HR inferred cortical power density

profiles that accurately matched the spatiotemporal behavior of the yolk membrane response. Indeed, the frontier between the active central contractile area, supplying mechanical power, and the surrounding stretched membrane, resisting to deformation, precisely correspond to the transition between inferred positive and negative mechanical power density regions (see **Appendix Figure S3a**).

In second place, we further validated HR by examining a well-defined physical model, a spherical fluid droplet sedimenting in an immiscible liquid. For this model, the fluid velocity at low Reynolds number is analytically known (Guyon et al., 2001) (**Appendix Figure S4a**). Regression analysis was used to fit a modeled SC field created by placing Stokeslet pairs on a spherical shell to the known analytical solution (**Appendix Figure S4b**). We found that both, the simulated fluid flow and the dynamic pressure distribution inside the droplet reached a quasi-perfect fit (**Appendix Figure S4c**). HR also provided an estimate of the cortical stresses and pressure fields inside the fluid that were consistent with the measured interfacial surface tension. The values derived from the analysis were also in agreement with the force balance between the droplet surface and the fluid (**Appendix Figure S4d**).

Appendix Note S5. Preparation of embryos for AFM measurements *in toto*

Recently laid zebrafish embryos were dechorionated and mounted in glass bottom Petri dishes on a shallow bed of 0.5 % low melting agarose in E3 embryo medium with a thickness half the height of the embryos. This ensured that cortical tension measurements were not affected by the agarose used to hold the embryos. We measured the Young's modulus (E) of the agarose gel by recording three sets of five force curves atop the agarose surrounding one of the embryos. Since AFM agarose measurements were taken on a flat surface of a homogeneous elastic material, the force curves were analyzed with the contact Hertz model of a sphere indenting an elastic half-space (Rico, Roca-Cusachs et al., 2005),

$$F = (4/3) \cdot [R^{1/2} / (1-\nu^2)] \cdot E \cdot h^{3/2} \quad (49)$$

The agarose used to hold the embryos was very soft with E = 4.2 ± 0.2 Pa (mean ± SD). Substituting the T_c and E values in the liquid-droplet (see Equation 4 in Methods) and half-space (Equation 49 above) equations, respectively, the forces required to produce a given indentation to the agarose gel in the range applied can be estimated to be more than 20-fold smaller than those to the embryo. Therefore, the limited thickness of the agarose layer and its very low Young's modulus ensure that the force curves recorded atop the embryo were not affected by the surrounding agarose.

Appendix Note S6. Cortex ablation versus Membrane Damage

Pulsed laser surgery with a sub nanosecond laser was performed by thermionic plasma formation, which induces transient cavitation bubbles of very short lifetime and submicron size (Vogel & Venugopalan, 2003). The laser surgery process was very sensitive to local absorption of tissues and its efficiency was statistically variable. In our experiments, we witnessed two distinct reactions of the zebrafish yolk cortex: a weak cortex damage versus a stronger damage accompanied with membrane damage.

To analyze the difference between the two scenarios, we performed simultaneous fluorescence and bright field transmission imaging after surgery. In the first condition, low damage was brought to the cortex, yielding a short retraction width W and a wound healing process which progressed in two phases: first a myosin-enriched contractile disc forms around the wound (**Appendix Figure S5b**) and, second, myosin filaments flow inside the wounded area during the final closure (**Appendix Figures S5b** and **S5c**). Noteworthy, the shape of the wound did not significantly change during repair, remaining elongated in the direction of the cut. On the other hand, high damage inflicted: 1) a wider retraction width W (**Appendix Figure S5f**), 2) a wider myosin-enriched contractile disc and 3) a more persistent wounded area that did not show any recovery of myosin in its central area (see Kymograph in **Appendix Figure S5f**) and that underwent a significant change to a circular shape.

To characterize the difference between 'weak' and 'strong' damage, we correlated the fluorescence imaging sequences to simultaneously recorded bright field transmission

data. In the 'weak' damage scenario, we detected membrane ripples retracting away from the laser cuts (**Appendix Figure S5b**). Interestingly, we showed that myosin and membrane ripples retracted synchronously and together showing a strong mechanical connection between the cortex and the membrane (**Appendix Figure S5c**). In the 'strong' damage scenario, instead, an apparent hole in the membrane, typically accompanied with loss of yolk material (e.g. small granules) was observed (**Appendix Figure S5e**).

We further explored the difference between weak cortex damage and strong membrane damage by simultaneously imaging the dynamics of a membrane-bound fluorescent protein Tg (β-*actin:m-GFP*) with bright field transmission. After weak damage, the membrane label rapidly recovers to fill up the gap (**Appendix Figure S6b**), while stronger damage yielded an apparent hole during the wound repair (**Appendix Figure S6d**). This was corroborated with transmission images showing mild membrane-ripples retraction after weak cortex damage versus a physical opening of the membrane with lost of yolk material, after strong damage.

We conclude from these experiments that laser surgery can be driving two retraction dynamics: on one hand, a cortex relaxation with no apparent damage to the membrane, but nevertheless showing a contact between cortex and membrane. On the other hand, a stronger damage-induced membrane opening and wider relaxation effects. We have chosen to exclude the sequences showing strong damage from the analysis of cortex relaxation to avoid any potential artifacts introduced by important membrane damage.

Appendix Note S7. Epiboly simulation

The SC model was used to generate a simulation of epiboly according to the experimentally observed kinematics. We considered a spherical shell representing the cortical surface of the virtual embryo, set the EVL / yolk margin to its position at the onset of epiboly and imposed *ad hoc* β_e coefficients to the Stokeslet pairs to fit a simulated velocity field to the experimental velocity fields. The variation of Stokeslets strength, β_e, with their position along the dorso ventral axis (imposed in the simulation) accounts for the different stiffness of the EVL and yolk cortex. The exponential decay

of contractility is specifically restricted to the E-YSL by imposing positional limitations for this term. For each time step of the simulation, the longitudinal component of the velocity vector v* was used to shift forward the EVL / yolk margin

The cortical surface of the virtual embryo was represented by a sphere, the EVL margin (φ^*) set at specific positions for each time point and the parameters of the circular solutions imposed as a function of their distance to the margin position. The EVL margin was set at time point 0 at its position at the sphere stage (beginning of epiboly). The longitudinal component of the velocity vector at the EVL margin, v*, was used to displace it during sufficiently small time steps in sequential time points.

For the simulation, 16 circles with a symmetric distribution of Stokeslets dipoles of strength β_z were placed on the spherical surface. The magnitud of the parameters β_z were chosen to follow the predictions of the theoretical kymograph. Specifically they are parametrized as

$$\beta_z = ½ \, . \cos (\pi/2 + \varphi_z - \varphi^*) / \delta\varphi \qquad (50)$$

for the EVL, covering the surface of the sphere from the animal pole to the EVL margin ($\varphi_z - \varphi^* < 0$) and

$$\beta_z = ½ \, . \cos (\pi/2 + \varphi_z - \varphi^*) / \delta\varphi - 1 / 7 \, . (1 - \cot \varphi^*) / \delta\varphi \, . e^{-(\varphi^* - \varphi z) / \delta\varphi} \qquad (51)$$

for the yolk cortex, covering the surface of the sphere from the EVL margin to the vegetal pole ($\varphi_z - \varphi^* > 0$).

At the time point being simulated, φ_z identifies the angle of the corresponding circle where the dipole is located, $\delta\varphi$, the characteristic width of the E-YSL, and φ^*, the angle at which the EVL margin is positioned.

The first term, which applies both to the EVL and the yolk, simulates the difference of elastic tension between these two structures. Thus, $\varphi_z - \varphi^*$ is negative for the EVL and positive for the yolk cortex. The second term, applying only to the yolk cortex, takes into account the exponential contraction ($e^{-(\varphi^* - \varphi z) / \delta\varphi}$) of the E-YSL.

$\delta\varphi$ was set to linearly decrease from initiation until 70 % epiboly and then to remain constant until closure in accordance with the experimental measurement of the width of the E-YSL (**Appendix Figure S1**).

In this way, a 3D simulated velocity field in the cortex and surrounding fluid medium can be calculated at every time. From the velocity field, simulated values for the dynamic pressure, mechanical power density and local cortical surface tension were

obtained following the same procedure applied in the spherical HR analysis.

An equivalent approach was applied to infer the dynamics of the EVL front speed in differenty conditions. In particular, we explored the consequences of manipulating the decay of δφ (E-YSL width) by adjusting the contraction terms (**Figure 7a**). To increase precision, we employed 51 circles with a symmetric distribution of Stokeslets dipoles in these analyses. The EVL front speed is obtained averaging the component of the velocity along the dorso ventral axis in a narrow band of 5º around the position of the margin position.

Appendix Note S8. Extended Discussion on Hydrodynamics Regression Characteristics and Applications

Computational modeling has been employed to indirectly infer spatio-temporal force maps estimating static mechanical properties. Our results show that mesoscopic regression analyses based on hydrodynamics (HR) allow inferring the spatio-temporal distribution of mechanical parameters from time-lapse movies. This simple methodology can be directly applied to relevant morphogenetic processes. We first validated the technique analyzing the response of the zebrafish embryo external yolk membrane to laser injury, and further with the fluid droplet, an analytically established hydrodynamic system. In both cases the physical parameters (dynamic pressure fields, mechanical power densities and surface tension) inferred by HR strongly correlated to the expected values proving that HR can be applied to different geometrical configurations. Next, we applied HR to study the mechanical principles underlying zebrafish epiboly. In brief, as epiboly progressed, we identified the mechanically active structures and uncover a positive gradient of tension gradually developing at the cortex. These predictions were confirmed experimentally endorsing the suitability of HR as a tool for global mesoscopic analyses of morphogenesis biomechanics.

Surrounding fluids

HR demands that the fluids surrounding the cortex should behave as Newtonian.

However, even if surrounding fluids are non-Newtonian per se, this should not represent a problem for HR implementation at small strain rates at which non-Newtonian materials behave as Newtonian. Indeed, fluid Newtonian behavior at low Reynolds number is commonly accepted for developmental processes including the establishment of the body plan or organogenesis (*C. elegans*, *Drosophila*, *Xenopus* or mice) (reviewed in (Cartwright, Piro et al., 2009).

Further, a recent study in the one-cell *C. elegans* embryo states that if non-Newtonian properties were dominant in the cytoplasm, cytoplasmic flows could not be described, as they are, applying a MPS simulation using the Navier-Stokes equation with constant viscosity (Niwayama, Shinohara et al., 2011). These results indicate that a Newtonian fluid is a good approximation and thus, non-Newtonian properties appear to play a minor role in cytoplasmic streaming, at least in *C. elegans*. This finding is also consistent with a previous microrheology study showing that simple diffusion (Newtonian behavior) was observed in the cytoplasm of the *C. elegans* embryo, which performs as a viscous fluid under physiologically relevant amplitudes of applied force (Daniels, Masi et al., 2006). These authors suggest that many other biological flows may also be well described as Newtonian fluids. Indeed Indeed, in the context of epithelial folding during gastrulation in the early *Drosophila* embryo, stresses generated at the surface integrate with the hydrodynamic properties of the interior fluid, which behaves as Newtonian with a low Reynolds number, to transmit force (He, Doubrovinski et al., 2014).

In this scenario, our assumptions will be true for all biological fluids except for those that behave as Bingham plastics, which show phase transitions at small strains. If HR would be applied to Bingham plastics, which show phase transitions at small strain rates, the inferred stresses would be uniformly underestimated by a constant, the yield stress, whatever the strain rates. Still, this underestimation would not prevent applying HR when inferring relative stress differences or identifying stress gradients. Nonetheless, in the zebrafish, our experimental results indicate that the yolk does not undergo any plastic transition. If it would have, this transition would be reflected as a yield point in the stress-strain relationship and result in a marked fall in the slope of force-indentation curves recorded in the embryo with AFM. By contrast, we found that these curves exhibited a linear behavior for small strains indicating the absence of any significant plastic transition.

Would the yolk stop behaving as Newtonian beyond any particular strain rate threshold? The accuracy of the fitting of the yolk flows employing Stokes equation solutions at all times during epiboly strongly argues against this possibility. The yolk fluid seems to remain Newtonian all the time. Further, fitting accuracy also support the fact that the strain rates are small everywhere.

Cortex

Although, HR will infer power densities and stress tensors regardless of the cortex material properties, it is important to point out that the macroscopic response of many tissues is viscoelastic (where the tissue behaves as an elastic solid over short timescales and a viscous fluid over long timescales). Indeed, zebrafish explants of embryonic ectodermal tissues are viscoelastic (Schotz, Burdine et al., 2008). Explants aggregate under compression and behave like elastic solids on short scales (seconds). Long-term compression for one hour or more, however, leads to explants flattening upon compressive force release indicating they rearrange to dissipate the imposed stress, a characteristic typical of liquids. This transition timescale is probably tissue dependent.

Still, during epiboly in Xenopus (Luu, David et al., 2011), the ectodermal epithelium mimics an elastic solid when stretched isometrically at a time scale of hours *in vivo*. Considering that developmentally and geometrically amphibian and teleost epibolies are equivalent, and that not only do the relative values of their germ layer surface tensions fall in the same range but even their absolute values are essentially the same (Schotz et al., 2008), we would expect they will show equivalent mechanical properties.

Studies in *Fundulus* have suggested that the epibolizing EVL is under tension both around the circumference and along the animal–vegetal axis of the embryo. In zebrafish, EVL tissue spreading is accompanied by pronounced EVL cell flattening, as recognized by an increase in apical surface area and concomitant decrease in cell height along the apical–basal axis of individual EVL cells. Further, laser-cutting of the EVL cortex uncovers its anisotropic tension and indeed the EVL can be modeled as a continuous elastic medium in which tensions and elastic deformations occur at length scales that are large compared with that of individual cells (see (Campinho, Behrndt et al., 2013) and references therein).

On the other hand, the yolk cortex (this manuscript and (Behrndt, Salbreux et al., 2012)) and the EVL tissue (Campinho et al., 2013) retract after laser microsurgery, which demonstrates their elastic properties. We found that the relative tension at the surface varies as epiboly progresses and is different at distinct positions. However, in all cases, the elastic response of the cortex is sustained all along the process.

Applications

HR, in principle, could be applied to images acquired from any microscope including light-sheet fluorescence (Keller & Stelzer, 2008) or non-fluorescence non-linear microscopy (Second-harmonic generation - SHG and Third-harmonic generation - THG) (Supatto, Truong et al., 2011) providing velocity fields could be estimated. It does not depend on cumbersome and error prone image analysis techniques and relies on a well-established hydrodynamic model, which exploits the analytical expressions of elementary solutions of Stokes flow. These elementary solutions (pairs of Stokeslets) are distributed along the cortex geometry and oriented normal to it. Stokeslet pairs have been employed to reconstruct the flow around a beating cilium (Ainley, Durkin et al., 2008) and for parameter-free comparisons of hydrodynamic predictions during epithelial folding in *Drosophila* embryos (He et al., 2014).

Stokeslet pairs model local cortical contractions or expansions and are used to fit a simulated velocity field to the experimental velocity fields estimated by PIV. Due to the force balance between the cortex and adjacent fluids (see also **Appendix Note S2**), the cortical stresses are determined from the fluid velocity fields. Significantly, HR is largely over-determined; *i.e.* manage to fit a large number of variables with a small number of unknown parameters (the coefficients β_e associated to the elementary solutions). A major advantage is that the analytical dynamic pressure field is always unique for a given velocity field. Thus, any change in dynamic pressure distribution leads to different velocity fields, and *vice versa*. Finally, as the model is mesoscopic, potential microscopic inequalities, *e.g.* heterogeneities in the conformation of actin and/or myosin filaments in a network, are not directly estimated. However, HR opens the possibility to indirectly address spatial heterogeneities through the inhomogeneous strengths of the Stokeslet pairs.

HR enables to explore different model systems to infer dynamic pressure and mechanical power density maps as well as cortical stresses. It does not pose any restrictive assumption on the mechanical properties of the cortex (when applied to small deformations) (see above). The method is thus flexible enough to be adapted to most deforming tissues and morphogenetic processes. So far, we have considered tissues that lead to motion with a well-defined symmetry, both for PC and SC. However, the method is more general as the only symmetry that is central to it is the symmetry with respect to the measurement plane. HR could be applied in the absence of such symmetries if enough information on the motion of the fluid around the tissue of interest can be retrieved. If the velocity field is measured in 3D, then the restriction on regular cortex geometry can be relaxed. Overall, HR applicability does fundamentally relate to the structural and temporal properties of the process under study: the cortex can be modelled by a stretchable surface within incompressible fluids.

In comparing to HR, current image based analytical methods aiming at inferring pressure and tensional parameters seem severely limited. Most of them rely on the application of vertex models to planar epithelia. In these models, the geometry of cell junctions has to be extracted from image segmentation and it is assumed that the cell edge linear tensions and internal pressures are at quasi-equilibrium. To estimate the internal pressure of each cell and the tension of each cell-to-cell edge, two different approaches have so far been undertaken: 1) a statistical model of tension distribution (Ishihara & Sugimura, 2012) and 2) the solution, in the least square sense, of an over-determined system of equations imposing a common value for the internal pressure and cortical tensions of each cell (Chiou, Hufnagel et al., 2012). None of these methods account for deforming tissues as they model an epithelium at quasi-equilibrium, and hence can only probe static mechanical properties. As such, they cannot be easily applied to morphogenetic dynamic processes. On the other hand, Video Force Microscopy (VFM) (Brodland, Conte et al., 2010) stands apart and allows to derive 2D forces based on tissue deformations estimated from time-lapse videos using a finite element model. Here, the space is discretized and partial differential equations are constrained at the boundaries of each partition. In VFM, the system of linear equations is exactly determined and solved through matrix inversion. This method hence faces the typical error sensitivity inherent to inverse problems. So far VFM has only been applied in 2D settings and both, passive viscous dissipation and long-range pressure

propagation in the third dimension are disregarded. The pattern of tension simulated by the method cannot model any resisting or active part of the process outside the measurement plane, whereas HR can. We anticipate that as the method stands today, VFM would be unable to properly describe the patterns of flows inside the yolk during zebrafish epiboly or accurately map cortical power densities and stresses in 3D. Finally, quantitative measurements of cellular stresses within tissues have been recently achieved by shape reconstruction of injected microdroplets using confocal microscopy and image analysis (Campas, Mammoto et al., 2014). Local spatial inhomogeneities in cellular stresses can be measured with this technique, but it fails to measure the isotropic tissue pressure consequence of large-scale tissue flows. In some sense, this method may complement the information gathered by HR, and combining both methodologies could constitute a sound approach to analyze the overall biomechanics of developing tissues.

APPENDIX FIGURES AND LEGENDS

Appendix Figure S1

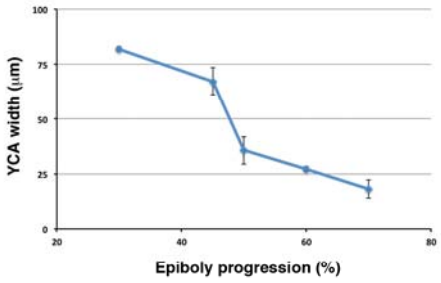

Appendix Figure S1. Width of the E-YSL over time

The E-YSL contracts during epiboly. Between 4.5 to 7.5 hours post fertilization, its width is reduced from 79 to 18 μm as an average. Values were calculated by measuring the width of the wrinkled area of the yolk surface of multiple embryos at distinct time points corresponding to different epiboly stages (30, 45, 50, 60 and 70 %). Error bars are displayed.

Appendix Figure S2

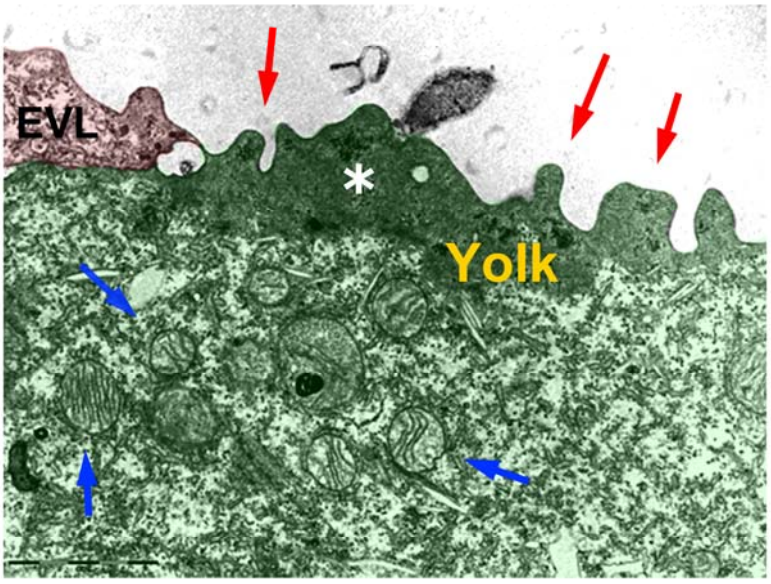

Appendix Figure S2. Ultrastructural analysis of the E-YSL

Transmission electron microscopy (TEM) section of the cortical yolk region (green shadow) confronting the EVL (red shadow) of an embryo at 70 % epiboly. Membrane wrinkles (red arrows) and abundant mitochondria (blue arrows) cluster at the presumptive E-YSL. A thick electron dense region (white star) that could correspond to unstructured actin underlines the cortical yolk wrinkles. Scale bar 2 μm.

Appendix Figure S3

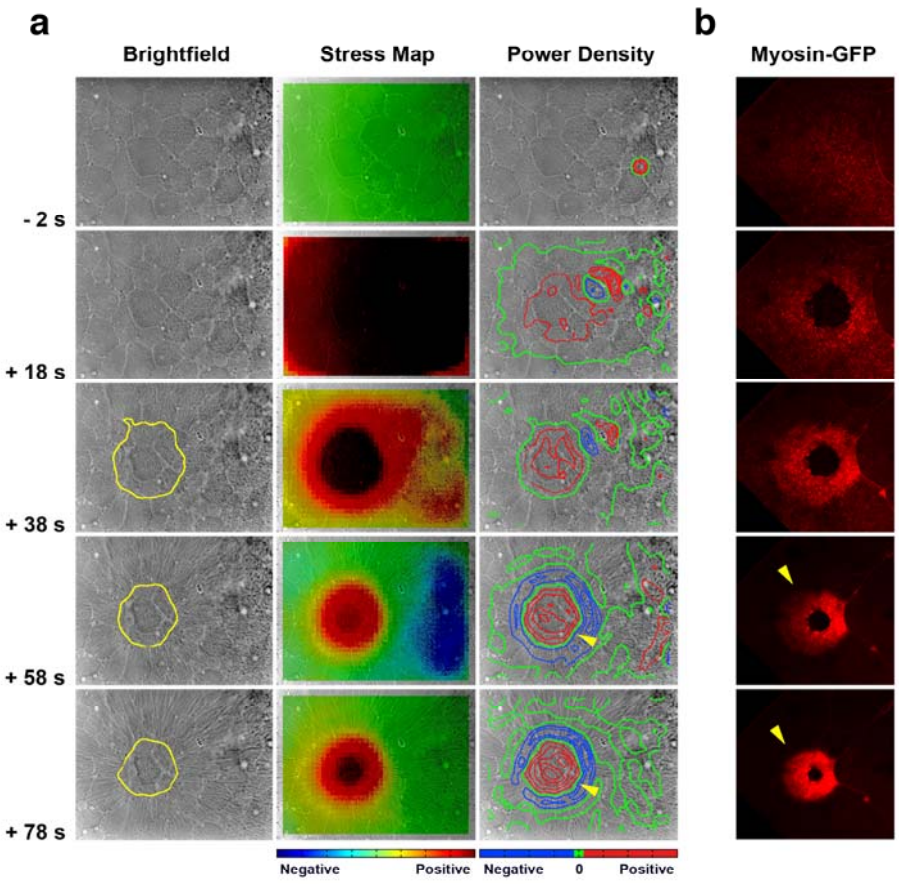

Appendix Figure S3. Planar Hydrodynamic Regression analyses (PC) of the response of the zebrafish yolk cortex to damage

(a) Planar regression analysis of the response of the yolk surface to laser damage (from **Video EV3**). Microscope bright field snapshots (left). Tangential stress maps were calculated for each time point by HR analyses color-coded and overlaid on the bright field images (negative - blue; 0 - green; positive - red) (middle). Surface power density color-coded level lines (negative - blue; 0 - green; positive - red) are charted on the (right). Before the cut (-2 seconds) the membrane is slightly wrinkled, no movement is observed and the dynamic stress and power are null (surface tension is at equilibrium). Immediately after the cut (+18 seconds) a long-range massive active contraction occurs and membrane wrinkling increased. The stress goes up all over the plane of view as a result of a local mechanical energy supply (right). Then a transition occurs (+38 seconds); a central constricting region (yellow outline – left) segregates from the surrounding area that doesn't work anymore. A disc of positive power (red - right) fits to the constricting area (+58 seconds). This disc is encircled by a ring of negative power (blue - right), which associates to the surrounding membrane under tension. The surface of the constricting disc becomes increasingly wrinkled and shrinks, while the surrounding membrane displays radial ripples denoting its elastic resistance (+78 seconds). The border between these two regions it parallels through time with the limit (pointed by yellow arrowheads) between positive and negative power (green - right). **(b)** Snapshots of a spinning-disc time-lapse video after laser surgery of the yolk cell membrane. The cut was performed at the cortex of a Myosin-GFP Tg (β-*actin:myl 12.1-e-GFP*) transgenic embryo. Shortly after surgery a myosin-enriched contractile disc (yellow arrowheads) forms around the wound, topographically correlating to the positive mechanical power density identified by HR.

Appendix Figure S4

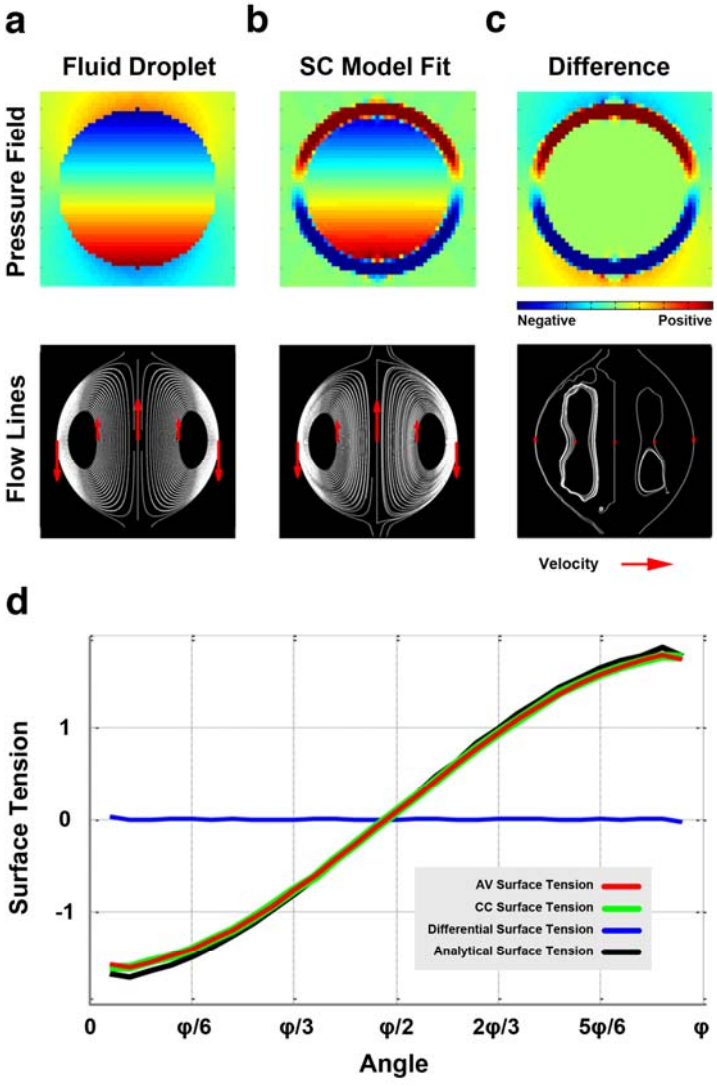

Appendix Figure S4. Spherical Hydrodynamic Regression analyses (SC) of the fluid droplet solution

Regression analysis fit to the sedimenting fluid droplet analytical solution (flow lines in white; velocity, red arrows; color coded dynamic pressure fields). **(a)** Fluid droplet analytical solution; **(b)** SC model fit by regression analysis; **(c)** difference between the fit and the fluid droplet analytical solution; **(d)** surface tension. The fluid droplet internal flows are reproduced by a spherical cortex under mechanical stress surrounding and surrounded by a viscous fluid. The result of the fit is quasi perfect (relative mean square error 0.00001 %), both for the internal flow and dynamic pressure field. The dynamic pressure gradient at the cortex induces the internal flow and allows to calculate the two perpendicular main components of the elastic surface tension (AV, red and CC, green) and their difference (blue), that were plotted as a function of the φ polar angle from animal (0) to vegetal (φ). We compare them to the surface tension calculated from the force balance at the boundaries between the fluid and the cortex (black; see **Appendix Note S2**).

Appendix Figure S5

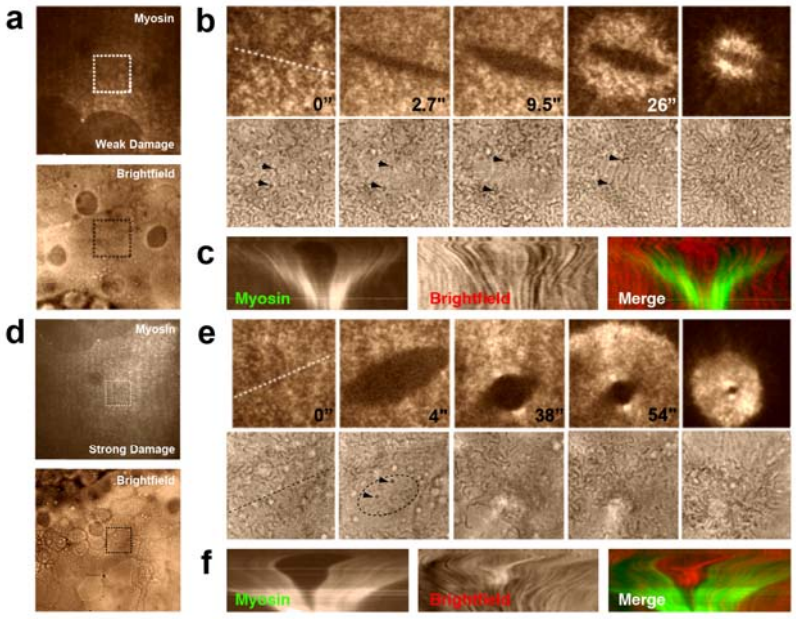

Appendix Figure S5. Laser surgery of the cortex versus membrane and cortex

Simultaneous fluorescence and bright field imaging of retraction and wound healing transients after laser surgery of the yolk cortex near the EVL of Myosin-GFP Tg (β-*actin:myl 12.1-e-GFP*) embryos. Two different types of injury can be induced: without membrane damage ('weak') and with membrane opening ('strong'). (**a-c)** 'Weak' injury. **(a)** Low magnification view (myosin staining – top; bright field - bottom) of the EVL front and injury area (dashed square). **(b)** Sequence of the response of the cortex along the dashed line (myosin staining – top; bright field - bottom). Retraction stops in less than 10 seconds and repair occurs within less than 2 minutes by contraction of a myosin-enriched disc and re-emergence of fluorescence inside the wounded area. Noteworthy, the wound shape is conserved during healing. **(c)** Kymographs (left: myosin; middle: bright field transmission; right: merge) showing the correspondence between myosin localization and membrane wrinkles after surgery. (**d-f)** 'Strong' injury. **(d)** Low magnification view (myosin staining – top; bright field - bottom) of the EVL front and injury area (dashed square). **(e)** Sequence of the response of the cortex along the dashed line (myosin staining – top; bright field - bottom). Retraction stops in less than 10 seconds and repair occurs by contraction of a wide isotropic myosin-enriched disc. The re-emergence of fluorescence inside the wounded area is not observed and the wound dramatically changes shape, becoming circular. Noteworthy, some granules near the cut are out-of-focus after the cut (encircled black arrows in (**e**), showing that material has come out of the embryo, an effect that is not visible in the 'weak' damage condition. **(f)** Kymographs (left: myosin; middle: bright field transmission; right: merge) showing a correspondence between myosin localization and membrane ruffles movements after surgery.

Appendix Figure S6

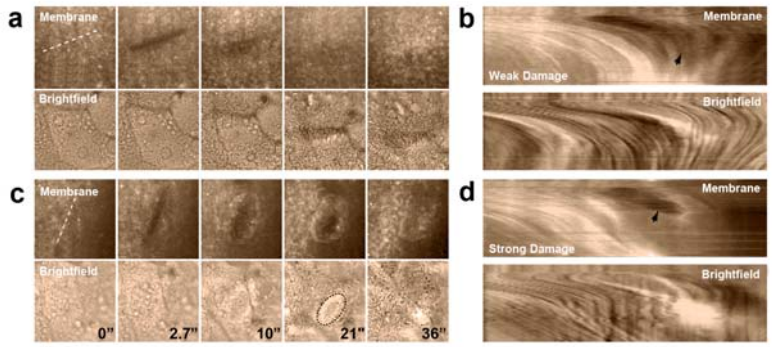

Appendix Figure S6. Membrane response to laser surgery

Simultaneous fluorescence and bright field imaging of retraction and wound healing transients after laser surgery of the yolk cortex near the EVL of membrane-GFP Tg (β-*actin:m-GFP*) embryos. Comparison of 'weak' and 'strong' laser cuts on membrane-behavior. **(a)** Sequence of response of the cortex along the dashed line after 'weak' surgery of the cortex as described in **Appendix Figure S5**. Fluorescence (top) and bright field transmission (bottom). The yolk cortex recovers within 10 seconds from the wound and the yolk membrane does not show evidence of damage. **(b)** Kymographs (top: fluorescence; bottom: bright field transmission) for 'weak' injuries showing membrane wrinkles retracting away. **(c)** Sequence of response of the cortex along the dashed line after 'strong' surgery of the cortex. Fluorescence (top) and bright field transmission (bottom). **(d)** Kymographs (top: fluorescence; bottom: bright field transmission) for 'strong' injuries showing a hole in the membrane, visible both in fluorescence [compare black arrows in (**b)** and (**d**)] and in transmission. The wound somewhat recovers at slower pace for 'strong' cortex injuries. Yolk material is projected out of the embryo (observed in **d**) (vertical features; i.e. immobile particles).

Appendix Figure S7

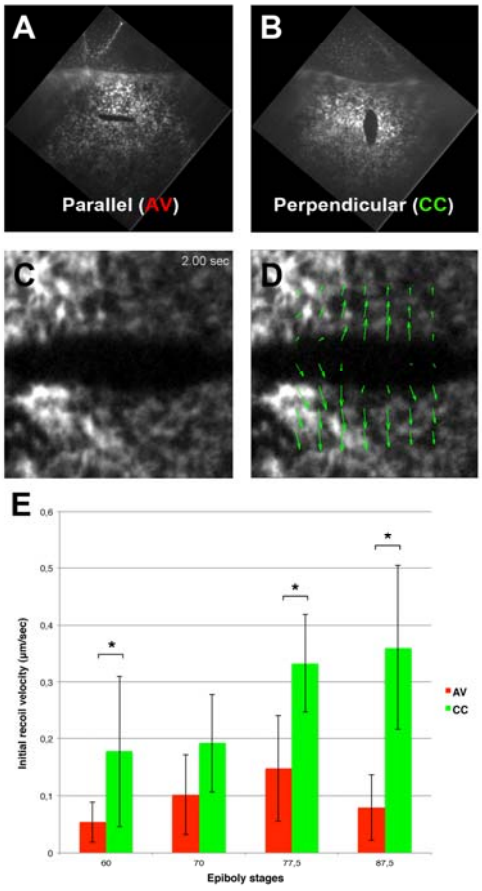

Appendix Figure S7. **CC and AV Retraction Velocities at the E-YSL**

(a, b) Parallel (AV) and perpendicular (CC) cuts in the yolk cortex of a Myosin-GFP transgenic embryo [Tg (β-*actin:myl 12.1-e-GFP*)] at 20 µm from the EVL margin. **(c, d)** Pre-processed image from a parallel (AV) cut and its overlaid PIV field (in green). **(e)** Retraction velocities (µm/s) determined from the PIV field (see Methods) for CC (green) and AV (red) cuts plotted over time. Laser cuts were performed from 60 % until 87.5 % epiboly. 60 % (CC – n = 29; AV – n = 19). 70 % (CC – n = 14; AV – n = 12). 75 % to 80 % (CC – n = 12; AV – n = 11). 80 % to 90 % epiboly (CC – n = 19; AV – n = 16). Significance differences between CC and AV stresses $p < 0.005$ are indicated.

Appendix Figure S8

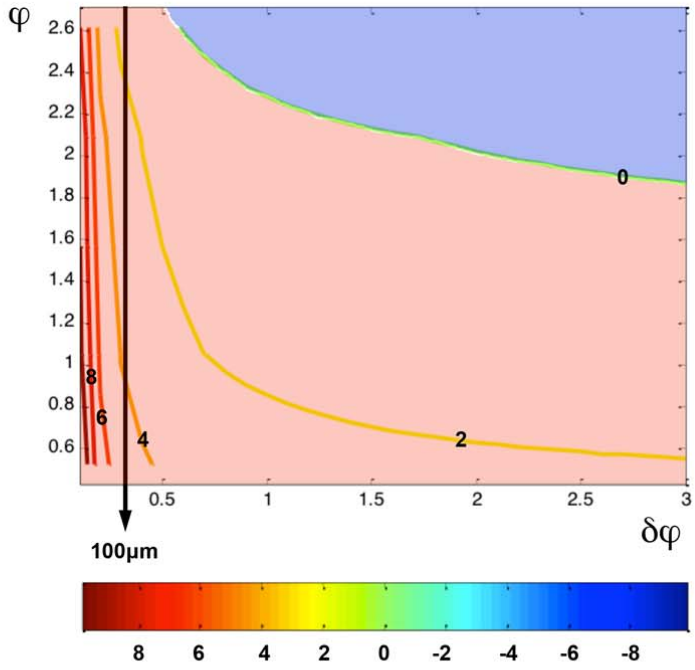

Appendix Figure S8. Level lines of 1/δφ + cotan φ as a function of δφ and φ

1/δφ + cotan φ graphs are represented for increasing values of **φ** (magnitude 0 (green) to 10 (dark red)coded as shown in the color bar at the bottom). The green line delineates the frontier between positive (lower left side – pink shadow) and negative values (blue shadow) in the δφ (x-coordinate) and φ (y-coordinate) space. As the width of the E-YSL is smaller than 100 µm throughout epiboly (black arrow), this term 1/δφ + cotan φ is always positive and the difference between AV and CC stresses in the E-YSL, $\sigma_{\varphi\varphi} - \sigma_{\theta\theta} = 2\,(e_{\varphi\varphi} - e_{\theta\theta}) = -\,2\,.\,v^{*} / R\,.\,(1/\delta\varphi + \text{cotan}\varphi)\,.\,e^{-(\varphi-\varphi^{*}) / \delta\varphi}$ is always negative.

Appendix Figure S9

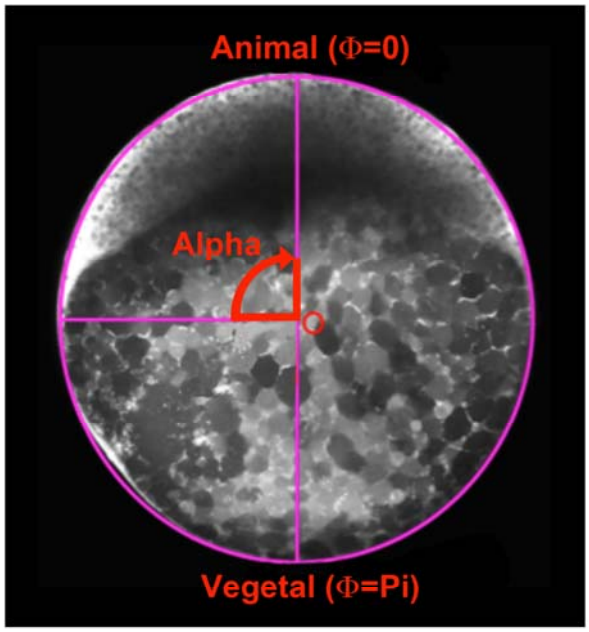

Appendix Figure S9. Embryo orientation for HR analysis

The tilt angle α is defined relative to the horizontal axis. A null angle corresponds to a situation where the animal pole is perfectly horizontally orientated and pointing to the left. As a convention we write these angles in the range [-2Pi ; 0]. On this figure the embryo tilt is 90 degrees (Pi/2 radians).

APPENDIX REFERENCES

Ainley J, Durkin S, Embid R, Boindala P, Cortez R (2008) The method of images for regularized Stokeslets. Journal of Computational Physics 227: 4600-4616

Behrndt M, Salbreux G, Campinho P, Hauschild R, Oswald F, Roensch J, Grill SW, Heisenberg CP (2012) Forces driving epithelial spreading in zebrafish gastrulation. Science 338: 257-60

Brodland GW, Conte V, Cranston PG, Veldhuis J, Narasimhan S, Hutson MS, Jacinto A, Ulrich F, Baum B, Miodownik M (2010) Video force microscopy reveals the mechanics of ventral furrow invagination in Drosophila. Proc Natl Acad Sci U S A 107: 22111-6

Campas O, Mammoto T, Hasso S, Sperling RA, O'Connell D, Bischof AG, Maas R, Weitz DA, Mahadevan L, Ingber DE (2014) Quantifying cell-generated mechanical forces within living embryonic tissues. Nat Methods 11: 183-9

Campinho P, Behrndt M, Ranft J, Risler T, Minc N, Heisenberg CP (2013) Tension-oriented cell divisions limit anisotropic tissue tension in epithelial spreading during zebrafish epiboly. Nat Cell Biol 15: 1405-14

Cartwright JH, Piro O, Tuval I (2009) Fluid dynamics in developmental biology: moving fluids that shape ontogeny. HFSP J 3: 77-93

Chiou KK, Hufnagel L, Shraiman BI (2012) Mechanical stress inference for two dimensional cell arrays. PLoS Comput Biol 8: e1002512

Daniels BR, Masi BC, Wirtz D (2006) Probing single-cell micromechanics in vivo: the microrheology of C. elegans developing embryos. Biophys J 90: 4712-9

Fisher RA (1922) The Goodness of Fit of Regression Formulae, and the Distribution of Regression Coefficients. Journal of the Royal Statistical Society 6

Guyon E, Hulin JP, Petit L (2001) Physical hydrodynamics. Oxford University Press,

He B, Doubrovinski K, Polyakov O, Wieschaus E (2014) Apical constriction drives tissue-scale hydrodynamic flow to mediate cell elongation. Nature

Ishihara S, Sugimura K (2012) Bayesian inference of force dynamics during morphogenesis. J Theor Biol 313: 201-11

Keller PJ, Stelzer EH (2008) Quantitative in vivo imaging of entire embryos with Digital Scanned Laser Light Sheet Fluorescence Microscopy. Current opinion in neurobiology 18: 624-32

Luu O, David R, Ninomiya H, Winklbauer R (2011) Large-scale mechanical properties of Xenopus embryonic epithelium. Proc Natl Acad Sci U S A 108: 4000-5

Niwayama R, Shinohara K, Kimura A (2011) Hydrodynamic property of the cytoplasm is sufficient to mediate cytoplasmic streaming in the Caenorhabditis elegans embryo. Proceedings of the National Academy of Sciences of the United States of America 108: 11900-5

Rico F, Roca-Cusachs P, Gavara N, Farre R, Rotger M, Navajas D (2005) Probing mechanical properties of living cells by atomic force microscopy with blunted pyramidal cantilever tips. Physical review E, Statistical, nonlinear, and soft matter physics 72: 021914

Schotz EM, Burdine RD, Julicher F, Steinberg MS, Heisenberg CP, Foty RA (2008) Quantitative differences in tissue surface tension influence zebrafish germ layer positioning. HFSP J 2: 42-56

Supatto W, Truong TV, Debarre D, Beaurepaire E (2011) Advances in multiphoton microscopy for imaging embryos. Current opinion in genetics & development 21: 538-48

Vogel A, Venugopalan V (2003) Mechanisms of pulsed laser ablation of biological tissues. Chem Rev 103: 577-644